JGR Oceans

RESEARCH ARTICLE
10.1029/2020JC016603

Effect of Cold Front-Induced Waves Along Wetlands Boundaries

Jin-Young Kim[1], James Kaihatu[1,2], Kuang-An Chang[1,2], Shih-Heng Sun[2], Thomas P. Huff[3], and Rusty A. Feagin[2,3]

[1]Zachry Department of Civil & Environmental Engineering, Texas A&M University, College Station, TX, USA, [2]Department of Ocean Engineering, Texas A&M University, College Station, TX, USA, [3]Department of Ecology and Conservation Biology, Texas A&M University, College Station, TX, USA

Key Points:

- Slow-moving cold fronts lead to more energetic waves in confined bays and greater potential for salt marsh erosion
- Wetlands inundation caused by coincident cold front-driven water levels and high tide weakens the impact of energetic waves on marsh edge
- Forcing spectral wave models with wind gusts, rather than averaged winds, leads to improved predictions of cold-front driven surface waves when using default wave parameters in Simulating WAves Nearshore model

Correspondence to:
J. Kaihatu,
jkaihatu@tamu.edu

Citation:
Kim, J.-Y., Kaihatu, J., Chang, K.-A., Sun, S.-H., Huff, T. P., & Feagin R. A. (2020). Effect of cold front-induced waves along wetlands boundaries. *Journal of Geophysical Research: Oceans*, *125*, e2020JC016603. https://doi.org/10.1029/2020JC016603

Received 4 AUG 2020
Accepted 29 OCT 2020

Abstract Along wetland shorelines, the energetic wave environment generated by cold fronts occurs more frequently than for major storms, yet their impact on wetland evolution processes has not been fully identified. To capture the changes in wave climate during the passage of cold fronts, a wave gauge was installed near a salt marsh edge in Galveston Bay, Texas, USA. A coupled wave-hydrodynamic model, validated with the data, was used to assess the dominant processes of cold front induced surge and waves. During the measurement period, wind gusts and abrupt direction shifts during cold fronts produced high-energy wave events that propagated toward the wetland edge. Before a cold front passed our study area, there was an initial increase in the water level inside the bay. As soon as the cold front passed and the wind direction shifted, large waves were created by strong winds. Over the first few hours, the relatively high water level reduced the depth limitations on these waves, allowing them to be quite large. However, as the waves struck the wetland edge at these higher water levels, vegetation intercepted and dampened the erosive force. Over the next few days, the water level dropped well below the mean tide, allowing plunging waves to impinge directly on the edge with a high-energy flux. From the calculated wave power during the entire measurement period, it was found that cold front-induced waves, despite their brief duration, had a high erosive impact on the evolution of the wetland edge.

Plain Language Summary Wetlands around the world have been significantly eroded due to climate changes and human-induced local environmental changes. One of the causes of erosion is wind-driven waves impacting the wetland boundary. The passage of cold fronts over confined bays creates energetic waves and increases the water level, exacerbating the impact of these waves on wetlands despite the relatively short duration. These events are far more frequent than hurricanes, and thus have a likely higher impact on wetlands processes. To capture the changes in wave climates during the passing of cold fronts, a wave gauge was installed near the Galveston Island wetland boundary during December 2015. A series of computer models were used to reproduce the tide and wave conditions, and determine which processes were dominant during fronts. Passing fronts generated waves and increased the water level at the wetlands. The approaching waves impacted the edge of wetlands for most of the time period; at times, however, the wetlands were inundated by the increased water level and the wave impact was lessened. It was determined that, in general, the wave environment (and thus the erosion potential) appeared to be greater during the short-lived cold fronts than during times when no cold fronts were active.

1. Introduction

Salt marsh wetlands are an important component of coastal ecosystems. Marsh vegetation has a significant potential role as a barrier to storm waves (Fagherazzi, 2014; Möller et al., 2014). It also allows the enclosing estuary to act as a nursery habitat for numerous shellfish and fish species (Mathieson et al., 2000). Additionally, tidal hydrodynamics facilitate the transport of vital nutrients and tracers into and out of the wetlands (during flood and ebb tides), affecting both inshore and onshore vegetation and wildlife (Mann & Lazier, 2013).

However, tidal wetlands are continuously affected by sea conditions such as storm surge (Cahoon, 2006), natural and/or human-induced regional subsidence (van der Wal & Pye, 2004) and sea-level rise (Alizad et al., 2016). It has previously been shown that wind-wave activity near salt marsh wetlands is a potential

factor in accelerating wetland loss rates (Karimpour et al., 2016; Leonardi et al., 2016b; Marani et al., 2011; Schwimmer, 2001; Schwimmer & Pizzuto, 2000). Moreover, a combination of increased water levels and energetic wind-wave conditions can lead to additional wave breaking, amplifying the marsh edge erosion (Tonelli et al., 2010).

Numerous studies (Leonardi et al., 2016a, 2016b; Marani et al., 2011; Schwimmer, 2001) have shown a linear relationship between wave energy flux (or wave power) and lateral rates of salt marsh boundary retreat—this despite the possible complicating impacts of marsh root effects, soil characteristics, and bioturbation. The wave energy flux is strongly related to the volumetric erosion rates of the marsh edges and is considered a critical factor in overall marsh loss (McLoughlin et al., 2015). Moreover, frequent, moderately energetic weather conditions, rather than less-frequent extreme weather events (e.g., hurricanes), can have a greater impact on salt marsh retreat (Leonardi & Fagherazzi, 2015; Roberts et al., 1987; Roberts et al., 2015). Passing cold fronts are thus important drivers for shoreline changes of low-energy coasts (Keen, 2002). Despite recent progress in linking the wave power to marsh erosion, the connection to cold fronts is still not well studied.

Cold fronts are generally active from autumn to spring and move from north to south in the northern hemisphere (DiMego et al., 1976). These fronts are accompanied by gusty winds that can cause energetic waves over water. Winds ahead of a cold front along the Gulf Coast tend to arrive from the south and southwest, and then shift toward the northwest after the frontal passage. Subsequently, coastal water levels would change because of cold front-driven currents and Ekman transport before and after the arrival of northwest winds with the frontal passage. Cold front-driven currents are mainly caused by across-Gulf coast winds that can drive across-shelf flow to shallow bays. Ekman transport is caused by the balance between along-Gulf coast winds generated stress and Coriolis force in the deep water and the direction of the flows is directed 90° clockwise rightward with respect to the wind direction (Fagherazzi et al., 2010; Tilburg & Garvine, 2004; Walker & Hammack, 2000).

The water level increase in shallow tidal basins can cause a monotonic increase in wave power, thus causing additional potential marsh edge erosion (Fagherazzi & Wiberg, 2009; Valentine & Mariotti, 2019; Young & Verhagen, 1996). However, this increase in wave power with water level is true up to a point; further increase in water level can reduce erosion rates by weakening the wave thrust (defined as the depth-integrated dynamic pressure due to waves) at the edge of the salt marsh when the wetland platform is submerged. If the instantaneous water level is higher than the height of the edge of the wetland, the wave thrust on the wetland decreases sharply due to wave "overshoot" (Tonelli et al., 2010; Valentine & Mariotti, 2019). Subsequently, these overshooting waves become attenuated in the marsh platform due to the underlying vegetation, and thus no additional lateral erosion occurs (Möller & Spencer, 2002; Möller et al., 2014). As such, the wave and water level both needed to be considered simultaneously to evaluate the erosion potential of wetlands.

Hydrodynamic and wave models have been applied to evaluate the lateral erosion of salt marsh in shallow bays. Fagherazzi and Wiberg (2009) simulated wave evolution in shallow tidal basins based on the formulation presented by Young and Verhagen (1996). McLoughlin et al. (2015) and Priestas et al. (2015) compared the shoreline changes of the Virginia Coast (USA) to the wave model results based on the numerical model Simulating WAves Nearshore (SWAN) (Booij et al., 1999).

In areas populated by coastal wetlands, such as the barrier islands in shallow bays, wind-driven currents, and astronomical tides jointly control water fluxes (Duran-Matute et al., 2016; Lester et al., 2002). To model this, a large-scale hydrodynamics and wave model is necessary. In previous studies, coupled ADCIRC-SWAN models were applied to identify changes in the coastal environment under hurricane conditions in the Gulf of Mexico due to waves, tides, and surge inundation (Hope et al., 2013; Kerr et al., 2013; Sebastian et al., 2014). Hurricane-induced hydrodynamics and morphological changes in wetlands areas were also investigated by Liu et al. (2018) using the Delft3D model. However, no prior work has been done to model the impacts of cold-front-induced waves and hydrodynamics to the salt marsh boundary in a shallow bay.

In the present study, we utilize a large-scale coupled modeling system (Delft3D) to investigate processes (including wind, surge, and waves) in Galveston Bay along the Texas coast induced by two different cold

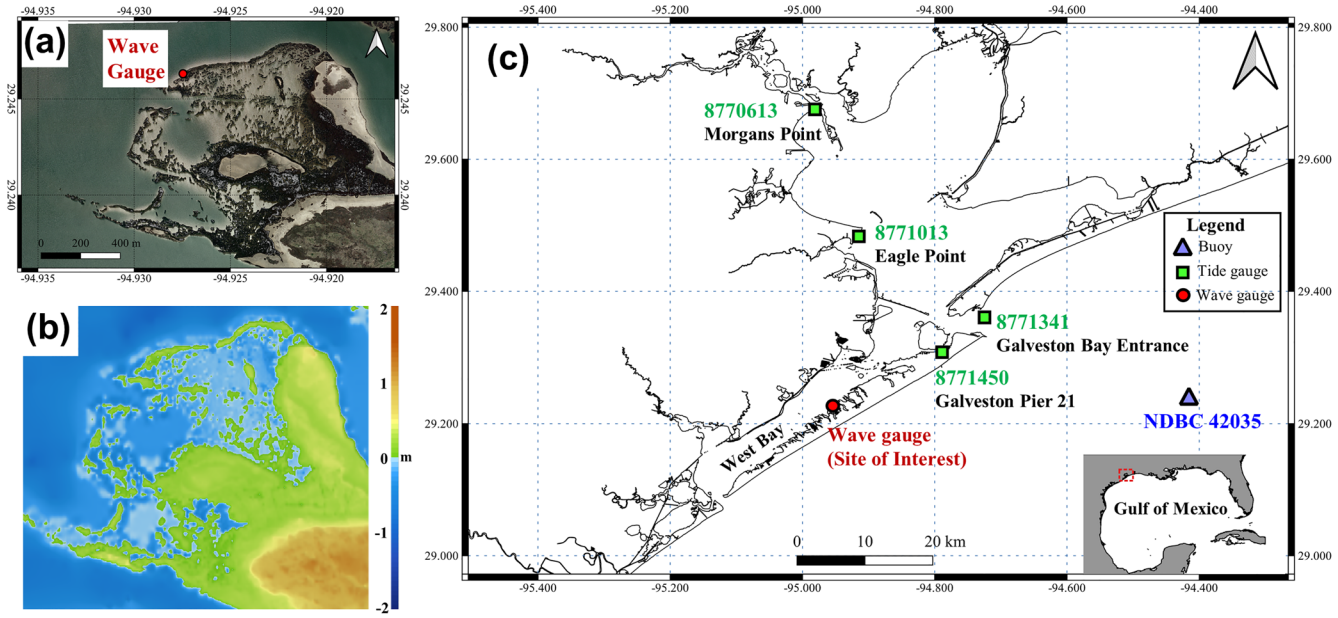

Figure 1. (a) Image of the Galveston Bay wetland at the study site, along with tide and wave gauge location (Source: NOAA NGS, 2011), (b) Topography and bathymetry of the study site in the model, and (c) locations of tide gauges and buoy around Galveston Bay used for model validation.

front passages. The model is also validated with in-situ data, an advance over many similar previous studies.

The purpose of this study is to show how cold front-driven wave and water level changes impact marshes and affect potential marsh edge erosion rates in coastal microtidal bays such as Galveston Bay. The objectives of this study are threefold: (1) to investigate the meteorological condition changes during the cold front passage that affect the wave and hydrodynamic environment in Galveston Bay; (2) to investigate the wave response to these fronts (and attendant impact on erosion), with a focus on the impact of wind gustiness during cold front passage; and (3) to quantify the effect of inundation in the marsh boundary areas on wave energy during times of simultaneous high tide and cold-front driven surge.

2. Study Area

2.1. Site Description

Galveston Island is a barrier island on the Texas Gulf Coast, located about 80.5 km southeast of Houston, Texas, USA. The island stretches 43.5 km long by 4.8 km wide at its widest point. The island is oriented northeast-southwest, with the Gulf of Mexico bordering on the east and south, West Bay and San Luis Pass on the west, and Galveston Bay toward the north (Figure 1c). The bay has an average water depth of 1.8 m with respect to mean sea level. West Galveston Bay is classified as a micro-tidal lagoon. Along the immediate shorelines of Galveston Bay, *Spartina alterniflora* grows. This plant is well-known for its extensive roots and below-ground production, and grows along many of the world's bay shorelines (Feagin et al., 2009). The platform elevation of salt marshes along the area was calculated to range from 0.3 to 0.45 m NAVD88 in both LIDAR imagery and survey-grade GNSS (Feagin et al., 2010; Kulawardhana et al., 2015).

A field site was established on the bayside of Galveston Island along West Galveston Bay. The site is located between Melager Cove and Oxen Bayou, about 6 km from Galveston Island State Park (Figure 1a). This site was chosen since it is typical of eroding north-facing barrier island wetlands, and is therefore exposed to the impacts of northerly winds from cold fronts.

The wetlands in the area are affected by mixed (diurnal and semidiurnal) tides and waves generated by cold front winds acting across the 6 km (width of West Bay) to 26 km (length of a northeast-southwest line

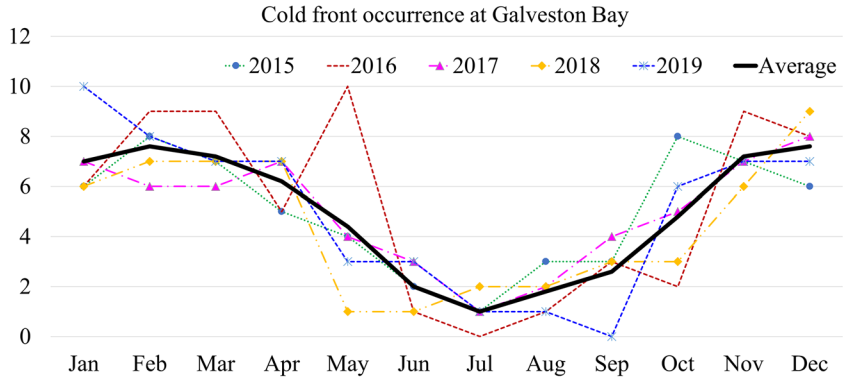

Figure 2. Monthly cold front passage at Galveston Bay between 2015 and 2019 and its all year average.

delineating the long axis of West Bay) fetch. Northerly winds may lead to water level difference as high as 1.0 m between east and west sides of the bay (Lester et al., 2002).

The loss of Galveston Bay salt marshes (estuarine marshes) has occurred at a rate of 0.7% from 1979 to 2002 (White et al., 2004). This is higher than the national wetland loss, estimated to be about 0.5% (59,400 acres) annually in the decade before 1986 (Dahl & Johnson, 1991). From 2006 to 2011, a total of 5.1% of Galveston county wetlands (yearly average 1.02%) have been eroded in terms of surface area (Entwistle et al., 2018). The majority of losses were the result of subsidence, sea-level rise, wave action, sediment deficit, dredging, and filling (Moulton, 1997; Ravens et al., 2009). Across our study location, the long-time rate measured by Gibeaut et al. (2003) from 1930 to 1995 was 0.58 m per year (Feagin et al., 2010). This rate includes shoreline facing both the predominant fetch direction and peripheral, protected shorelines. The rate accelerated in the later portion of this time range, largely due to sea level rise (Ravens et al., 2009). For shorelines facing the predominant fetch direction only, we also measured the lateral erosion rate using Google Earth images for dates from 1954 to 2018 and found a consistent linear rate with minimal outliers, arriving at 1.13 m per year. On these same stretches of shoreline, Huff et al. (2019) also recorded erosion in the field, also finding 1.13 m per year.

2.2. Cold Fronts Passage on Galveston Bay

From September to May, Galveston Bay is influenced by cold fronts, evidenced by a sudden drop in temperature and strong gusty winds highly variable in direction. After the cold front passage, the Galveston Bay area experiences cool and dry weather brought by the northerly or westerly winds. These changes affect the wave and circulation of the Galveston Bay system. The change in hydrodynamic conditions due to cold fronts in the Galveston Bay were discussed in Cox et al. (2002).

Changing environmental conditions associated with cold front passages can be classified as prefrontal, frontal passage, and postfrontal (Roberts et al., 2015). The mean water level of Galveston Bay is strongly influenced by cold front-driven currents, in addition to the astronomical tide. As the front approaches the coast, winds become more southerly which causes the water level to increase slightly, due to the influx of water from the Gulf of Mexico (prefrontal). Immediately after the cold front passage (frontal passage), the northerly or westerly wind dominates over the entire bay; there is a resulting drop in water level as the water in the Galveston Bay fetch is pushed to the offshore side (postfrontal).

The number of cold front passages from 2015 to 2019 are shown in Figure 2. The number of cold fronts that passed through Galveston Bay from 2015 to 2019 was determined based on the analysis of infrared satellite imagery produced by the Weather Prediction Center of NOAA. Analysis consisted of manual recognition and counting of surface front locations passing through the Galveston Bay, and was performed at 3-h intervals. Most of the cold fronts moved from North to South or from Northwest to Southeast. During the period, the months where the cold front passed most often were from November to February. From June to August,

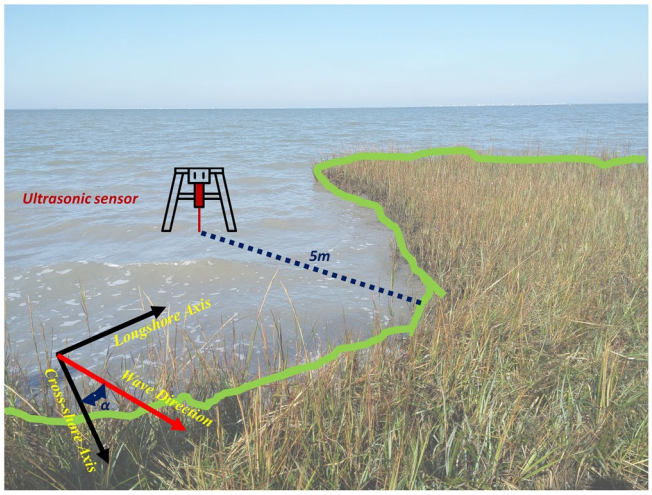

Figure 3. Sensor configuration and wetland boundary demarcation at the field site. Local coordinate system also shown.

the lowest number of cold frontal passages were observed. The average return period of the cold fronts in Galveston Bay was calculated as 6 days during the months in which they occur. Cold front gust generation, their directionality, and their forcing of waves are quantifiable, so it is important to investigate the effect of waves generated by these climatic events on the salt marsh.

2.3. Field Measurements

The study site, located at 29°14′46.55″*N* and 94°55′38.26″*W*, is near Melager Cove (Figure 1a), where the salt marshes present along the West Galveston Bay side of Galveston Island are exposed to northerly winds and waves. To measure wave energy, an ultrasonic wave sensor (T30UXUB, Banner Engineering, Inc.) was placed approximately 5 m offshore from the edge for a duration of nine days (December 10 to December 18, 2015), with a sampling rate of 20 Hz with no bursts (Figure 3). During this period, a large range of sea state conditions was encountered, with wind arriving from every direction and speeds ranging from 1.6 to 10.8 m/s, arising across a maximum fetch of approximately 6.25 km (the width of West Bay near the site).

Spectral wave analysis was performed for the water elevation records. The total record period is 8 days, 7 h, 16 min, and 28 s. The time series are divided into 1,993 realizations of 7,200 data points apiece, resulting in frequency bins of 4097 with a resolution of 0.0025 Hz. Each realization is input into the periodogram function, which yields the frequency vector. This function computes the FFT from the input water elevation vector. These initial spectra were truncated at $f_{\min} = 0.05$ Hz, as the signal errors and some unrealistic low-frequency parts were recorded during the frontal edge crossing mainly caused by the increased water level. The high-cutoff frequency was set equal to $f_{\max} = 1.00$ Hz. The average water level data was extracted by applying a moving average of 72,000 data points (1 h) window to the raw ultrasonic gauge data.

2.4. Wave Power (Wave Energy Flux)

Schwimmer (2001) found that the marsh regression rate is correlated to the averaged wave power, defined as:

$$P_w = \left(\frac{\rho g H_s^2}{8}\right) C_g \tag{1}$$

where H_s is significant wave height ($H_s = 4\sqrt{m_0}$, m_0 being the zero moment integral of the power spectrum), ρ is the water density, and C_g is the wave group velocity, where:

$$C_g = \frac{1}{2}\sqrt{\frac{g}{k}\tanh(kh)}\left(1 + \frac{2kh}{\sinh(2kh)}\right) \tag{2}$$

where k is wave number ($k = 2\pi/\lambda$, λ being the wavelength). The wavelength λ is calculated using the mean absolute wave period $T_{m-1,0}$ ($T_{m-1,0} = m_{-1}/m_0$, m_{-1} being the −1 order moment integral of the power spectrum) based on the dispersion relation ($\omega^2 = gk\tanh(kh)$, where $\omega = 2\pi/T$). The mean absolute average wave period (often called a mean energy wave period) is used to determine the wave energy flux per unit of wave-crest length (Hofland et al., 2017). For a marsh edge oriented at an angle to the wave propagation direction, the instantaneous incident wave power density is:

$$P_i = P_w \cos\alpha \tag{3}$$

where α is the mean wave direction relative to the direction normal to the marsh edge. Because the wave direction cannot be deduced using a single gauge, the P_i was calculated using the wind direction records at the Eagle Point wind station for the effective wave power calculation in the measurements, under the assumption that the waves are collinear with the wind direction. The average wave direction is assumed to be very close to the averaged wind direction records, and it is not considered to be a source of error since the direction of wind and waves were very similar in the model results. In addition, $P_i < 0$ represents times when the winds are directed away from the marsh edge, and as such do not generate waves that impact it; for these occurrences we set $P_i = 0$. The water depth at the site was not sufficiently small for the shallow water approximation of the linear dispersion relation to be used. The time series of the significant wave height, H_s, water level, and mean energy wave period, $T_{m-1,0}$, extracted from the wave gauge time series data, were used to calculate the C_g in Equation 2. The short distance between the gauge and the wetland edge would not allow for additional wind-wave generation, so the wave energy at the gauge was assumed to be representative of what occurred at the marsh edge. Wave reflection from the edge of the steep wetlands would likely be detected by the gauge; however, since it is a single gauge, there would be no way to extract it from the time series. While this reflection is not modeled, its neglect is not expected to be a significant source of error since the effective wave power value does not include waves directed away from the marsh edge.

Based on findings from Tonelli et al. (2010) and McLoughlin et al. (2015), we calculated the effective wave power by setting $P = 0$ when the extracted averaged water level was above the top elevation of the marsh edge platform. In a later section, we define three wetlands platform thresholds for calculation of effective wave power in line with this prior work. However, this definition excludes frictional effects generated by wavefront orbital velocity passing through the edge of a wetland, which can affect the salt marsh edge erosion (Karimpour et al., 2016). Other studies consider this effect by exponentially reducing the wave thrust as water level increases above the marsh scarp (Donatelli et al., 2019; Leonardi et al., 2016b).

3. Numerical Models

3.1. Model Description

Due to this study's focus on wind-generated waves, a phase averaged wave energy (or action) balance model is required. The SWAN model (Booij et al., 1999) is widely used for coastal regions and was used here. SWAN was used with DELFT 3D-FLOW within the DELFT3D model suite, thus allowing coupled wave and hydrodynamic modeling.

The DELFT3D-FLOW module solves the unsteady shallow-water equations in two (depth-averaged) or three dimensions (Lesser et al., 2004). The system of equations consists of the horizontal momentum equations, the continuity equation, the transport equation, and a turbulence closure model. The vertical momentum equation is reduced to the hydrostatic pressure relation as vertical accelerations are assumed to be small compared to gravitational acceleration and are not taken into account. Although the 3-D model has the advantage in resolving the vertical flow structure, a validated 2-D model can achieve similar accuracy in tidal current prediction with much higher computational efficiency (Horstman et al., 2013). Therefore, the 2-D version of the Delft3D model was used in the study to focus on depth-averaged currents in the shelf-bay-wetland system. In addition, we employed domain decomposition in the Delft3D-FLOW model. Domain decomposition is a technique in which a model is divided into several smaller model domains, with parallel computation occurring among all domains. In simultaneous computation with SWAN, nesting from a coarse grid to finer grids is used. In the outer boundary of the Gulf of Mexico grid, periodic conditions are applied at the open ocean boundary along the entrance of the Gulf of Mexico. Astronomical tidal constituents (K_1, O_1, Q_1, P_1, M_2, S_2, N_2, and K_2) are forced on the open ocean boundary using the TPXO 8.0 tidal atlas (Egbert & Erofeeva, 2002).

3.2. Bathymetry and Grids

For improved fidelity of the model, four model grids, spanning from the Gulf of Mexico to the wetlands in the bayside of Galveston Island, were adopted. The bathymetric grid for the Gulf of Mexico (Figure 4,

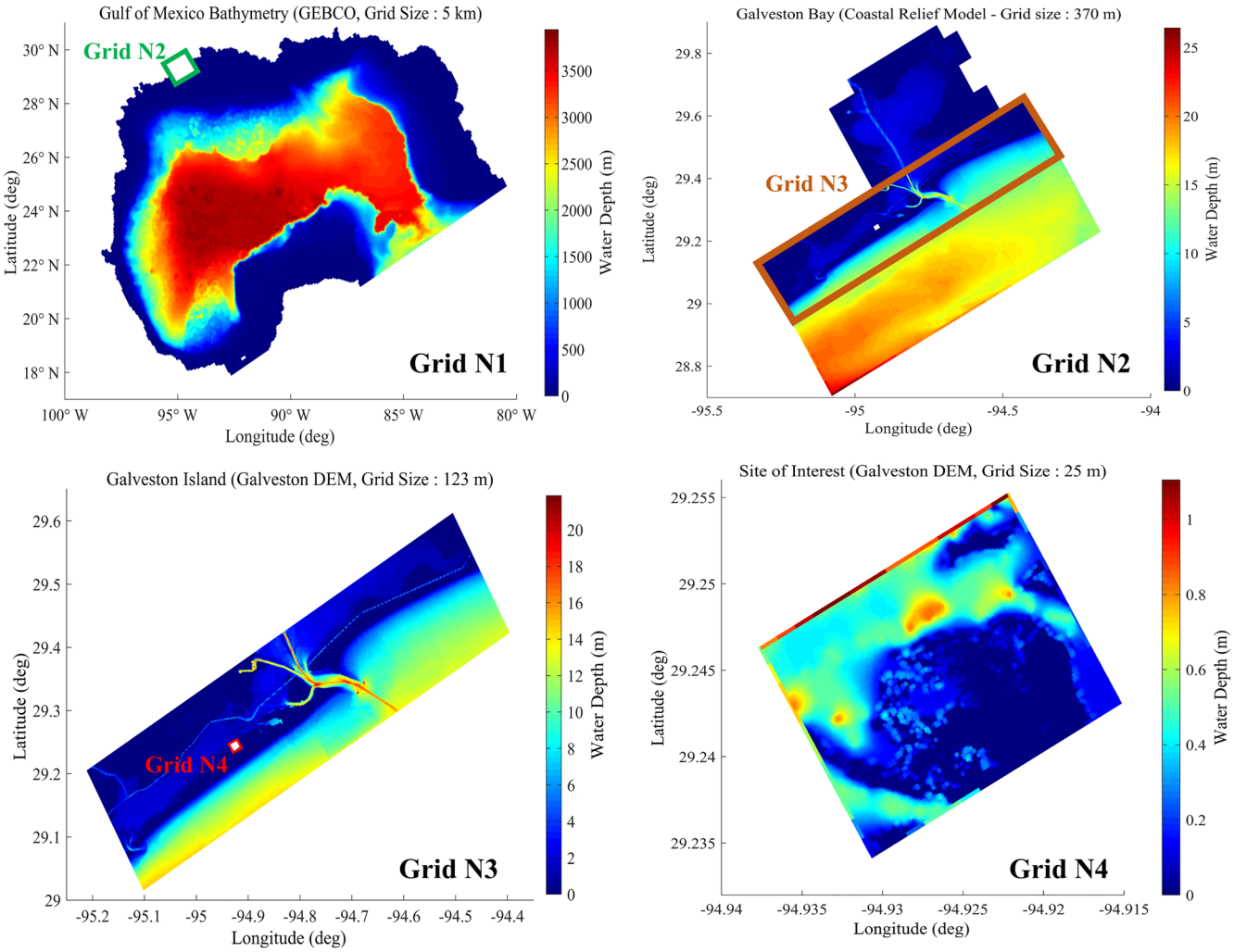

Figure 4. Model grid and bathymetry of Gulf of Mexico (N1), Galveston Bay (N2), Galveston Island (N3), and study area (N4) in Delft3D-FLOW and Simulating WAves Nearshore (SWAN) model.

Grid N1) was based on GEBCO-08 (Becker et al., 2009), a global bathymetry and elevation database at 30 arc seconds spatial resolution. The bathymetric grid for Galveston Bay (Figure 4, Grid N2) was constructed using a nearshore digital elevation model at 3 arc -second spatial resolution (U.S. Coastal Relief Model, National Centers for Environmental Information NOAA, U.S. Department of Commerce, Boulder, CO, September 2010). For Galveston Island (Figure 4, Grid N3) and the site of interest (Figure 4, Grid N4), the Galveston Digital Elevation Model 1/3 arc-second (10 m) high-resolution topography and bathymetry (Taylor et al., 2008) was adopted for the representation of the salt marsh boundaries located at the bay side of Galveston Island (Figure 1b). Because the Galveston DEM was originally transformed to Mean High Water (MHW) level for the vertical datum, bathymetric and topographic data for Grid N3 and Grid N4 were adjusted to the NAVD88 Datum using NOAA Vertical Datum Transformation (VDatum) software (Parker et al., 2003). The difference between MHW and NAVD88 at the study site is 0.3 m. However, the uncertainty regarding the difference between the MHW level and NAVD88 presented on VDatum is 0.11 m.

Grid resolutions for the Gulf of Mexico, Galveston Bay, Galveston Island, and wetlands in the Galveston Island grid are 5 km, 370 m, 123 m, and 25 m, respectively. Each equidistant grid was rotated such that the positive x-direction is oriented 30° clockwise from the west-to-east direction. The datum of the bathymetric data is important, since the water depth defined by bathymetry is directly related to wave shoaling and refraction and thus to the wave power at the salt marsh boundary. It should be noted that the present model

resolution (25 m, Figure 4 Grid N4) cannot reasonably resolve the highly variable bathymetry around the salt marsh edge.

3.3. Wind Input

NCEP Climate Forecast System Version 2 (CFSv2) 6-hourly Products (Analysis data) were applied (Saha et al., 2014) for the entire Gulf of Mexico (Grid N1) as well as the offshore side of Galveston Bay. These winds had a spatial resolution of 0.205 degrees. The comparison showed good agreement between NCEP offshore winds and NDBC buoy Station 42035, located outside of Galveston Bay entrance.

For the N2, N3, and N4 grids, winds and gusts from the nearest NOAA weather station in Eagle Point (Station ID: EPTT2, 8771013), Houston, Texas, measured at 6 min intervals, were input to the model over the measurement period. Averaged wind speed was determined by a 2-min scalar average of 1-s wind speed measurements collected prior to each 10th hour. The wind gusts were determined from the maximum 5-s moving scalar average of wind speed that occurred during the previous 6 min at the station. Winds from Eagle Point, measured at 8.0 m above mean sea level, were corrected to the standard 10 m height (NOAA Tides and Currents, 2020). Scholes International Airport weather station (77551), Galveston, Texas, is located 7.3 km east of the wave sensor location in Galveston Island. However, this weather station has low-directional resolution and frequent data gaps, precluding its use for modeling. Wind data from Eagle Point and Scholes Field International Airport were compared to confirm the similarity between two locations. It is found that the difference between the Scholes Field International Airport data and Eagle Point data was minimal, particularly during the cold front passage.

3.4. Parameter Selection for Model

The DELFT3D model suite was configured to allow the hydrodynamic flow model (Delft3D-FLOW) and the SWAN wave model to communicate every 6 min during the simulation. The time step of the DELFT3D-FLOW model was 12 s and the SWAN time step and coupling interval with the flow is 6 min. The time step of 12 s was chosen as a compromise between the Courant number (<10 is recommended, Deltares [2013]) in Grid N4 bathymetry and computational efficiency. Hydraulic friction is parameterized in the DELFT3D-FLOW model using a spatially varying Manning's n value based on the water depth. Offshore, areas with sandy/gravel bottoms such as the Florida shelf are set to $n = 0.022$, and areas with muddy bottoms like the Texas-Louisiana shelf are set to $n = 0.012$ (Buczkowski, 2006). These values are applied at depths >5 m, and they are increased linearly to $n = 0.022$ toward the shoreline. The SWAN time step of 6 min is determined by the time interval of the wind input, allowing the immediate update of the wind velocity and the subsequent wind-wave conditions in the model. The wave directional spectra are discretized into 72 directional bins of a constant 5-degree width, and the frequencies are discretized over 24 frequency bins, in the range of 0.05–1 Hz, which is the default in SWAN. The hindcast uses the wind input formulation based on Snyder et al. (1981), the modified whitecapping expression of Rogers et al. (2003), and quadruplet nonlinear interactions via the discrete interaction approximation (S. Hasselmann et al., 1985). For the shallow-water source terms, depth-induced breaking is computed with a spectral version of the model of Battjes and Janssen (1978) with the breaking index $\gamma = 0.73$. Wave refraction is enabled in regions where the resolution of the bathymetry is sufficient to prevent spurious wave refraction. Both models were run on the same computational grid, thus eliminating the need for interpolation between models. In the study area, an inner nest was included in the simulations to provide higher resolution in the wetlands of Galveston Island. The nest position is shown in Figure 4. Additional details on the SWAN wave model design are as follows:

1. Stationary computations, with settings for numerics according to Rogers et al. (2003)
2. Default settings for nonlinear interactions Snl4
3. Bottom friction for JONSWAP (Hasselmann et al., 1973), set to 0.067 m^2s^{-3}

The time series of the significant wave height, H_s, mean absolute wave period, $T_{m-1,0}$, and averaged wave direction θ as outputs from the SWAN model, combined with the Delft3D-FLOW results of the water level time series, were used to calculate wave power.

3.5. Skill Metrics

Model validation was quantified using the following skill metrics: Root Mean Square Error (E_{RMS}, which is a measure of the magnitude of error, with an ideal value of zero), Coefficient of Determination (R^2, which describes how well a regression line fits a set of data, with an ideal value of one), Normalized Bias (which is a measure of the model's magnitude of overprediction or underprediction normalized to the observed value, with an ideal value of zero), Scatter Index (SI, The standard deviation of E_i is SI which indicates how much the predicted variation pattern deviates from the observed one, with an ideal value of zero), and Mean Normalized Error (E_{NORM}, which is the mean error normalized by the mean observed value, with an ideal value of zero; Hanson et al., 2009; Kerr et al., 2013). Taking N as the number of observation points in the time series and $E_i = S_i - O_i$ as the difference between the model result S_i and the observation O_i, the equation for Mean Normalized Bias is

$$\mathrm{Bias} = \frac{\frac{1}{N}\sum_{i=1}^{N} E_i}{\frac{1}{N}\sum_{i=1}^{N}\left|O_i\right|} \tag{4}$$

and the equation for SI is

$$\mathrm{SI} = \sqrt{\frac{\frac{1}{N}\sum_{i=1}^{N}\left(E_i - \bar{E}\right)^2}{\frac{1}{N}\sum_{i=1}^{N}\left|O_i\right|}} \tag{5}$$

Additionally, the equation for Mean Normalized Error is

$$E_{\mathrm{NORM}} = \sqrt{\frac{\frac{1}{N}\sum_{i=1}^{N}\left(E_i\right)^2}{\frac{1}{N}\sum_{i=1}^{N}\left(O_i\right)^2}} \tag{6}$$

4. Results

Two cold fronts were observed during the measurement period. Figure 5a illustrates the frontal passage and first cold front, approaching Galveston Bay around DEC 13, 2015 14:30 (UTC) with peak average wind speed of 14.2 m/s and gusting of 21.4 m/s. During the prefrontal phase, winds at Eagle Point are directed from south to north (arriving from 170° to 180°). As the leading edge passed the weather station, the primary wind direction quickly changed to northerly (arriving from 320° to 360°) (Figure 5b). A drop in temperature of 8.5°C was recorded at the weather station after the frontal passage. A maximum gust of 10 m/s was recorded during the postfrontal phase. Gusty winds continued for nearly 7 hours from the frontal passage.

The second front approached Galveston Bay around 12:00 (UTC) on DEC 16, 2015 (Figure 6a), with a peak average wind speed of 10.2 m/s and gusts of 13.1 m/s. In contrast to the first cold front, this second front was oriented close to parallel to the shoreline. It also passed slowly over the region relative to the first cold front. The speed of winds coming from the south during the prefrontal phase of this second cold front was also lower relative to the first cold front. After the frontal passage, the gusty winds accompanying the cold fronts continued from December 16, 2015 12:00 to December 17, 2015 20:00 (UTC), overall duration of 32 h of northerly gusts winds whose directions ranged from 360° to 35° (Figure 6b) during the postfrontal phase. During this period the range of gusts was recorded from 5 to 11 m/s.

Figure 7 shows the measured and simulated water levels at the tide stations at Galveston Bay (Figure 1c). The measured water level showed a 0.6 m overall tidal range, with diurnal variation, at the site. From December 13, 2015 00:00 (UTC), wind-driven currents by prefrontal winds were shown to increase the overall Galveston Bay water level by approximately 0.2 m. Due to cold front-driven currents and coincident high astronomical tide, the water level over the measurement period was highest during the passage of the first cold front at December 13, 2015 12:00 (UTC), and lowest at December 14, 2015 23:00 (UTC). The metrics

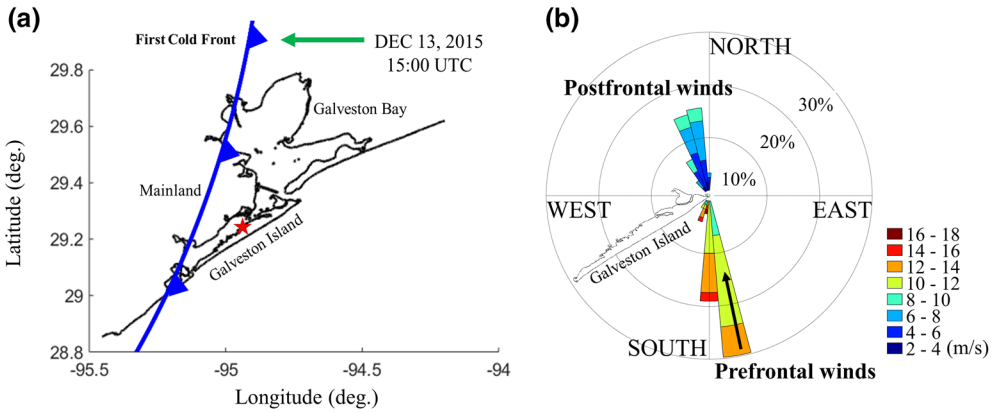

Figure 5. (a) History of movement and (b) Eagle Point (8771013) wind rose during the first cold front (May 13, 2015) across the coast of Texas.

reflecting the accuracy of the modeled water level in the tide stations are summarized in Table 1. The model results show accurate predictions during most of the measurement period. However, some discrepancies in water level records at the Galveston Bay Entrance and the Galveston Pier 21 tide stations were apparent. It is thought that this is due to the lower temporal resolution of wind conditions in the N2 grid (wind input: NCEP model) at the Galveston Bay entrance compared to the N3 grid (wind input: Eagle Point wind records).

To evaluate the effect of gusts on wave generation in West Galveston Bay, the model was run using the wind gust record and the results compared to that using averaged wind. The comparison also confirmed the wind data suitable for cold front-induced wave model prediction in the SWAN model. Significant wave height results forced by both the average wind data and wind gust data input were compared to measured significant wave height data, as shown in Figure 8. Use of the wind gust record as input results in better prediction ($R^2 = 0.68$) than use of the averaged wind as input ($R^2 = 0.45$). Therefore, the model result forced by wind gust input was used for all comparisons with the measurement result to be described later here.

Water level results in Figure 9d shows the measured and simulated water level changes during the measurement period at the site of interest as well as the generated water level signal from the widely used global astronomical tide model TPXO 8.0. As seen in the water level records, winds from the south during the prefrontal phase served to increase the water level (wind set-up) of the entire extent of Galveston Bay. The water elevation was the highest during the approach of the first cold front at December 13, 2015 12:00 (UTC). Both cold fronts passed through Galveston Bay during the end of the high astronomical tide condition, maximizing the water level of the Galveston Bay area. Under maximized water level conditions, it is likely

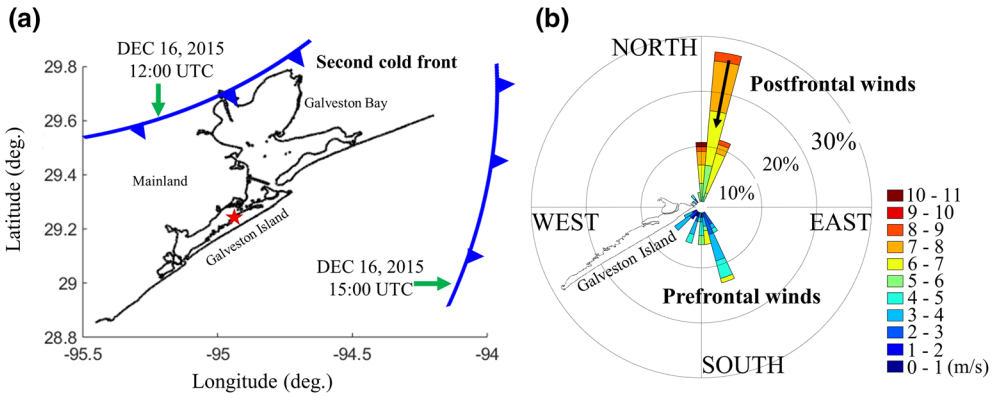

Figure 6. (a) History of movement and (b) Eagle Point (8771013) wind rose during the Second cold front (May 16, 2015) across the coast of Texas.

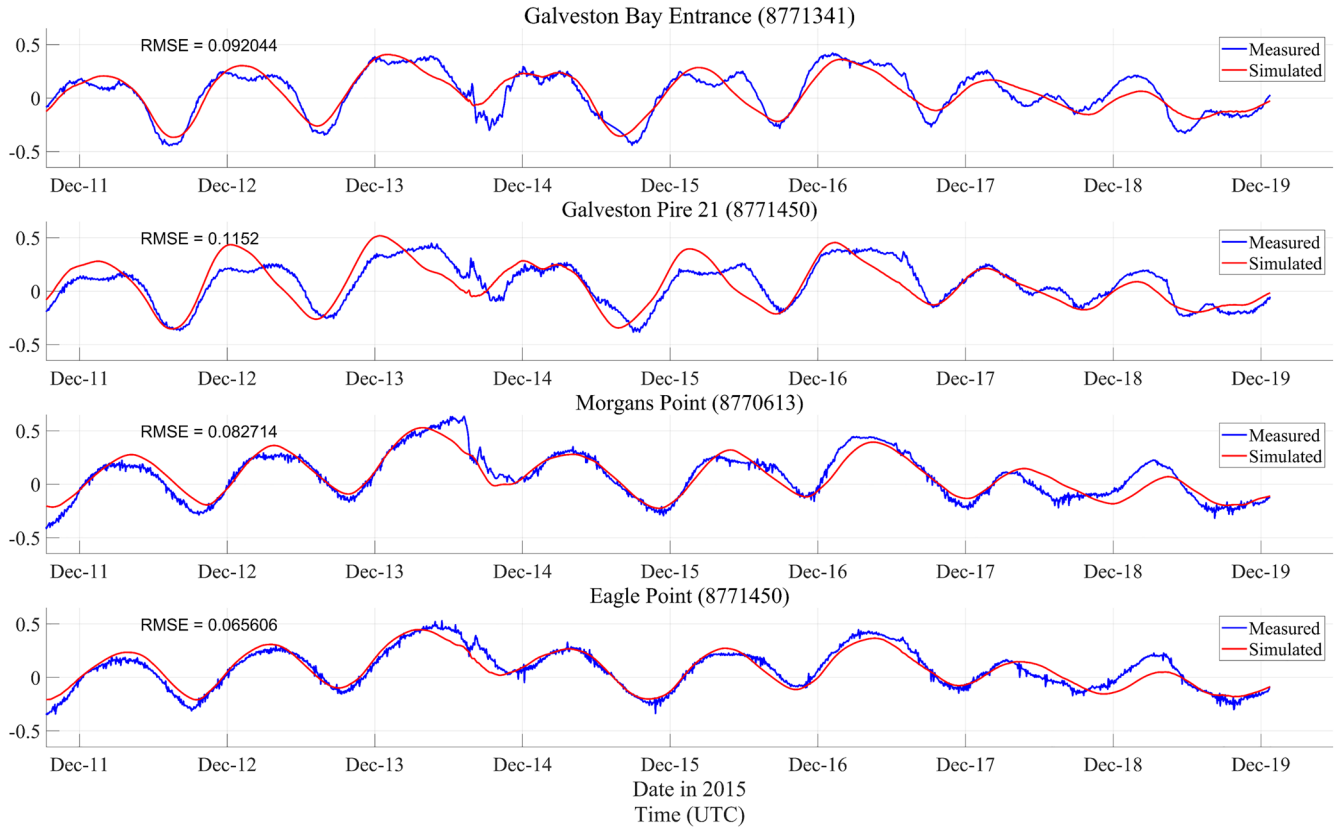

Figure 7. Measured and simulated water levels at tide stations in Galveston Bay.

that the wetlands boundary area switches from partially depth-limited conditions to entirely fetch-limited conditions. The lowest water level occurred around December 15, 2015 00:00 (UTC), which accompanied a low tide. The result of the significant wave height at the site of interest is shown in Figure 9 along with the wind inputs.

From December 11 to December 12, significant wave heights were less than 0.1 m at the site even though most of the wind speeds were above 5 m/s during this period. This is because most of the winds were not directed toward the salt marsh boundary. In the prefrontal phase of the first cold front, from December 13, the southerly wind speed increased from 5 to 10 m/s, and the wind arrived from the south which increases the influx of water into Galveston Bay. However, the significant wave height only increases from 0.05 to 0.1 m, likely due to the winds moving away from the north-facing wetlands.

During the frontal passage, a peak wind gust value of 20 m/s was recorded. The maximum significant wave height recorded during the first cold front passage in the model was 0.29 m.

In the postfrontal phase, wind speeds decreased significantly after the leading edge of the front passed the Galveston Bay area. The significant wave heights dropped to a very low level on December 14; from December 14 to 16, the significant wave height was below 0.1 m.

The second cold front, observed December 16 and 17, abruptly changed the wind velocity; it was accompanied by gusts and generated 0.12–0.21 m significant wave heights during the passage on December 16. The gusty winds lasted almost 2 days at the site and the wave direction was close to the direction normal to the salt marsh boundary. During the postfrontal phase after the second cold front passage, the TPXO 8.0 tide model

Table 1
The Accuracy of Model Predictions of Water Level Time Series

	Water level (m)				
Geographic location	$E_{RMS}(m)$	*SI*	*Bias*	R^2	E_{NORM}
Galveston Bay Entrance	0.09	0.005	−0.21	0.81	0.45
Galveston Pier 21	0.11	0.005	−0.17	0.65	0.60
Eagle Point	0.07	0.000	−0.44	0.88	0.45
Morgan Point	0.08	0.001	0.29	0.85	0.45
Site of Interest	0.04	0.006	−0.68	0.88	0.61

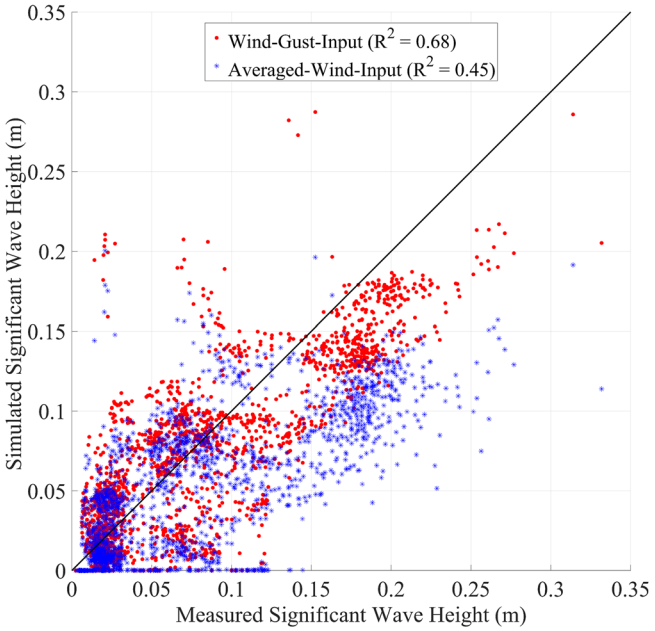

Figure 8. Comparison of modeled significant wave height results at the site of interest to the measured significant wave height results between two different wind inputs (Gust and Averaged wind).

showed low tide on December 17 at 00:00 (UTC). During this low astronomical tide condition, the significant wave height slightly decreased to below 0.12 m.

The accuracy of model predictions of significant wave height time series is summarized in Table 2. The model performance between two different wind inputs at the site of interest are also presented in Table 2. The average of E_{RMS} (m) and R^2 of the best fit of water level at all of the stations were 0.08 and 0.81, respectively.

The modeled significant wave heights and mean wave directions for different phases of the cold front passage are presented in Figure 10. The trend of mean wave direction change between the first cold front and second cold front period was very similar. However, the waves during the first cold front passage were more energetic (Figures 10b and 10e). During the postfrontal phase, the significant wave height of the second cold front was slightly higher than the first cold front (Figures 10c and 10f) and the duration of the postfrontal phase of the second cold front lasted longer.

Wave power calculated from the SWAN model results was tested against the observed wave power at the wave gauge deployment site. For the calculation of the effective wave power in the simulation, the water depth of the nearest marsh edge grid point most similar to the depth at the measurement was used. In addition, the direction corresponding to that of the mean spectrum was used as the wave direction results in SWAN

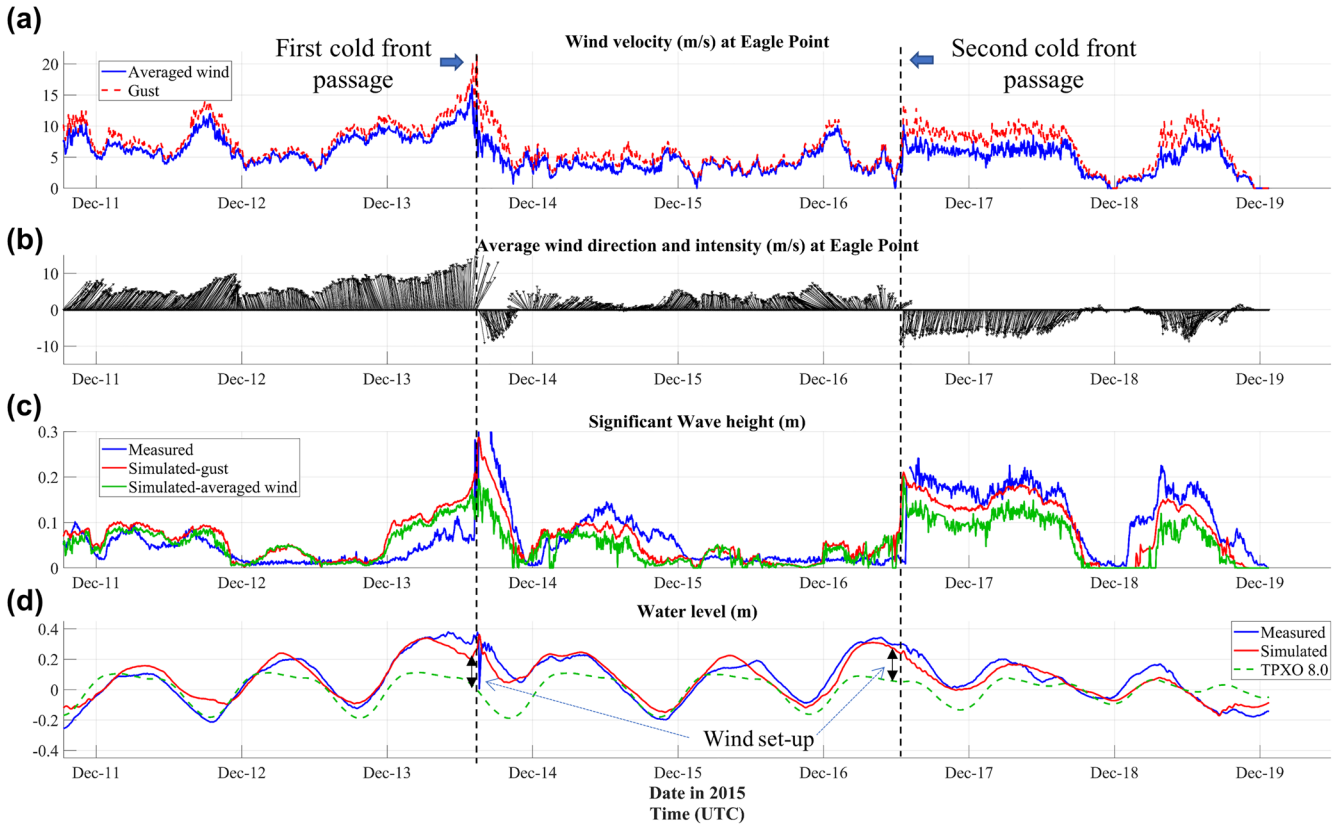

Figure 9. (a) Averaged wind velocities and wind gusts at Eagle Point, (b) averaged wind direction records at Eagle Point, (c) Comparison of significant wave height results between measured and modeled records, and (d) results of measured and modeled water level records compare to TPXO8.0 model.

Table 2
The Accuracy of Model Predictions of Significant Wave Height Time Series

	Significant wave height (m)				
Geographic location	$E_{RMS}(m)$	*SI*	*Bias*	R^2	E_{NORM}
Site of Interest (Gust)	0.03	0.001	0.00	0.68	0.40
Site of Interest (Ave. Wind)	0.03	0.006	−0.26	0.45	0.53
NDBC-42035	0.17	0.021	−0.42	0.83	0.42

for the calculation of the wave power. For the calculation of the effective wave power in the measurement, wind direction records of the Eagle Point winds were used to represent the wave direction. The modeled bulk wave power includes wave energy from all directions, whereas effective wave power only contains wave energy directed toward the edge of the wetland.

In addition to effective wave power, inundation of the wetlands required consideration since the flooding of the wetlands to elevations higher than the marsh edge elevation can reduce the erosion of waves (termed "overshooting"). However, to determine the marsh elevations, a detailed topographic survey of marsh edge elevation based on NAVD88 datum would be required; such a survey is not available. We did initially investigate LIDAR elevation data, and in general the marsh is quite flat in this location. Still, to illuminate the effect of inundation without this data, three estimated inundation cases were calculated for the estimation of the wave effect at the marsh edge while inundated. The water depth at the site immediately after sensor installation (December 10, 2015 18:36:00 [UTC]) was approximately 0.1 m, and the maximum water depth during the measurement period was 0.72 m. Data loss due to the extreme high tide exceeding the wave gauge measurement range occurred twice during the measurement period, which means at least two inundation events were observed. Based on the model grid of the marsh edge platform, inundation can be determined, but the simulated records might not represent the actual inundation at the site due to the inability to resolve the distance between the instrument and the marsh edge at

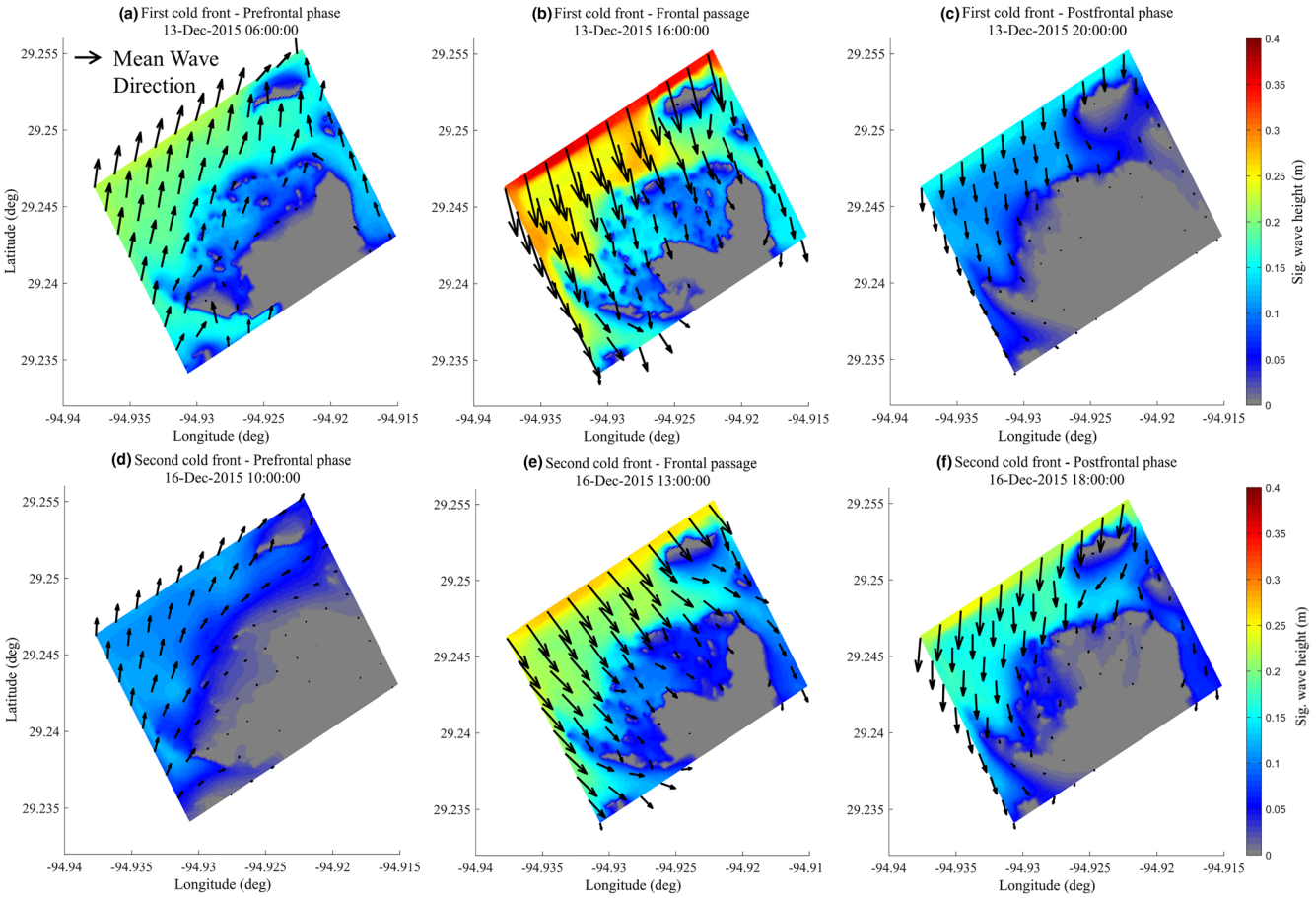

Figure 10. Significant wave height and its direction in different phases during the first cold front passage, (a) December 13, 2015 06:00 UTC (prefrontal phase), (b) December 13, 2015 17:00 UTC (frontal passage), (c) December 13, 2015 20:00 December (postfrontal phase) and during the second cold front passage, (d) December 16, 2015 10:00 UTC (prefrontal phase), (e) December 16, 2015 13:00 UTC (frontal passage), (f) December 16, 2015 18:00 UTC (postfrontal phase).

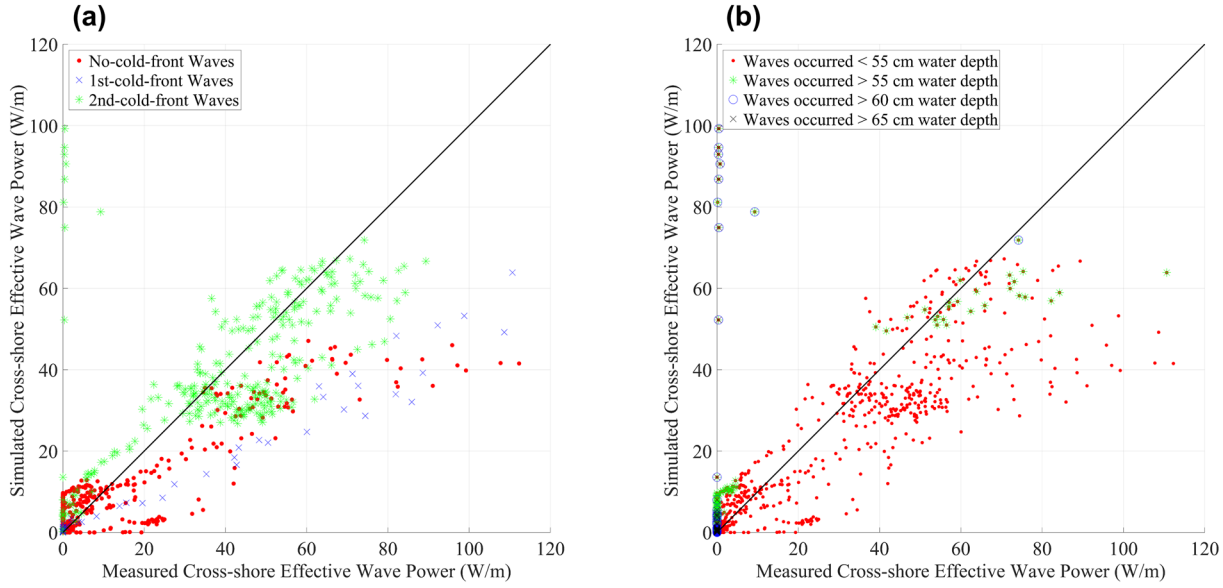

Figure 11. Comparison of effective wave power between measurement and model based on the "no-cold-front" period and cold fronts period (a) and classification of effective wave power based on different water depth thresholds (b).

the present grid cell size (25 m). To account for this, the critical water depth at which flooding of the marsh platform occurs (thereby nullifying the wave energy impact on the marsh) is set to three values of 0.55, 0.60, and 0.65 m, which were estimated based on measured water depth.

The comparison between the measurements and the modeled results for cross-shore components of wave power during the entire time period is shown in Figure 11. Underestimation of the modeled effective (shore-normal direction) wave power shown in Figure 11 is seen in the slightly underestimated significant wave heights and mean absolute wave periods in the model results. Wave power estimates during the second cold front have a lower wave power range of 40–60 (W/m), compared to the range of 40–110 (W/m) from the first cold front. However, the inundation caused by the strong southerly winds during the prefrontal phase of the first cold front reduced the impact of the high-wave power (Figure 11b). In contrast, the second cold front had a longer duration, and a relatively low-water level, exacerbating the impact of the wave power on the marsh edge. The values in the y-axis in Figure 11b represent the waves in measurements during the extremely high-water depth, abnormal data recorded due to exceeding the gauge measurement range, excluded in measurement records here. These values are considered to have minimal effects on the salt marsh lateral erosion since they have occurred during extreme high water depth.

5. Discussion

5.1. Sources of Model Input Uncertainty

The results from the DELFT3D-FLOW and SWAN model show accurate predictions of the water level oscillations and significant wave heights during most of the measurement periods at the site. Some disparity with measurements of significant wave height was found, especially during December 13, the prefrontal phase of the first cold front. The likely cause of the model errors was the spatial difference between the model output location and the location of the measurement since the 25 m grid resolution was coarser than the 5 m distance between the measurement location and marsh edge. Because of this disparity, the modeled results likely included more waves in the opposite direction of the salt marsh edge. It is believed that the significant change in topographic data by wetlands shoreline retreat around the study site between 2007 (when the topographic survey was done) and 2015 (measurement period) could have also contributed to the discrepancy between the modeled and observed significant wave height. The salt marsh erosion for the change in the estuarine hydrodynamics is considered to influence tidal amplitude and asymmetry. Moreover, the marsh

deterioration can reduce the sediment stock in back-barrier basins and therefore compromise the resilience of salt marshes (Donatelli et al., 2020). Bathymetric data fit to the 25 m resolution grid around the wetlands boundary could also cause inconsistency in the significant wave height calculation since there would likely be discrepancies in shoaling rates and wave breaking locations between model and measurement. Wind input used in the model was also 7 km away from the site of interest, which may cause errors in simulating the modeled wave properties. A significant difference in wind velocity during December 11 was found, but differences in averaged winds and wind gusts during the cold front passages were minimal. Moreover, the SWAN model usually overestimates the wave energy for waves of lower wave height; causing a discrepancy in significant wave height difference. Seibt et al. (2013) determined that SWAN simulations with measured wind fields tend to overestimate waves with low-wave amplitudes and to underestimate waves with higher wave amplitudes regardless of the modification of the specified parameters. The SWAN results in this study using default parameters for JONSWAP bottom friction (=0.67 m^2s^{-3}) and depth-induced wave breaking γ ratio (=0.73) also showed this tendency in the significant wave height results. In this study, the wind gust data that was used was slightly higher than the averaged wind during the cold front passages and may offset the effect of underestimation of the significant wave heights.

5.2. Characteristics of Cold Front Induced Wave Climate

A similar pattern of cold front induced hydrodynamic forcing was observed in the water level and the significant wave height during prefrontal, front passage, and postfrontal phases. Both the water level and significant wave height were highest at the end of the prefrontal phase. High water level conditions during the prefrontal phase allowed the generation of larger significant wave heights, which were critical to the potential marsh edge erosion. However, this situation was abated by the fact that the marsh edge is completely inundated by the higher water level. It is hypothesized that the wave energy affecting the marsh edge is highest when the water level is equal to or just above the marsh edge ground level, and that the wave environment along the north-facing marsh at the site is most energetic during the postfrontal phase of cold fronts. During the second cold front, higher significant wave heights in the postfrontal phase continued for 2 days with minimal (or no) inundation after its passage at the Galveston Bay. This combination of strong waves and lower water levels allowed the marsh edge to be intercepted with greater wave energy for a longer duration. The wind direction was usually close to shore-normal relative to the north-facing marsh edge immediately after the frontal passage and during the postfrontal phase, and this period had the most critical effect on the potential erosion of the marsh. However, it should be noted that the favorable model comparisons realized by using gust wind input may be related to the characteristics of the default wave generation mechanisms and parameters employed in this study.

5.3. Potential Impact of Model Results

To analyze the most significant likely cause of the marsh erosion at the site of interest, cumulative effective wave power from both measurement and model during three periods (“No-cold-front," first cold front, and second cold front) are shown in Figures 12a and 12c. To distinguish wave power invalidated by the inundation of the marsh platform, four immersion thresholds (No inundation, 0.65, 0.60, and 0.55 m) are also presented.

Overall, the measurements and model values were in good agreement. Because only one wave gauge was used, the wave direction was not measured but instead assumed to be the same as the wind direction. This can lead to potential errors in the measurement results of effective wave power. However, according to the results of the model, the errors were considered minimal, especially during the passage of the cold front since the wave direction closely coincided with the wind direction when the winds blew in the same direction for more than a given time. From the cumulative effective wave power results (Figures 12a and 12b), it was likely that cold front induced waves were a significant driver of potential marsh edge retreat in the Galveston Bay wetlands considering its short duration (first cold front—24.6 h, second cold front—30 h). The first cold front showed the highest wind gusts for a relatively short time, but after its passage, the duration of the postfrontal phase over which the waves approached the marsh boundary was short. This results in

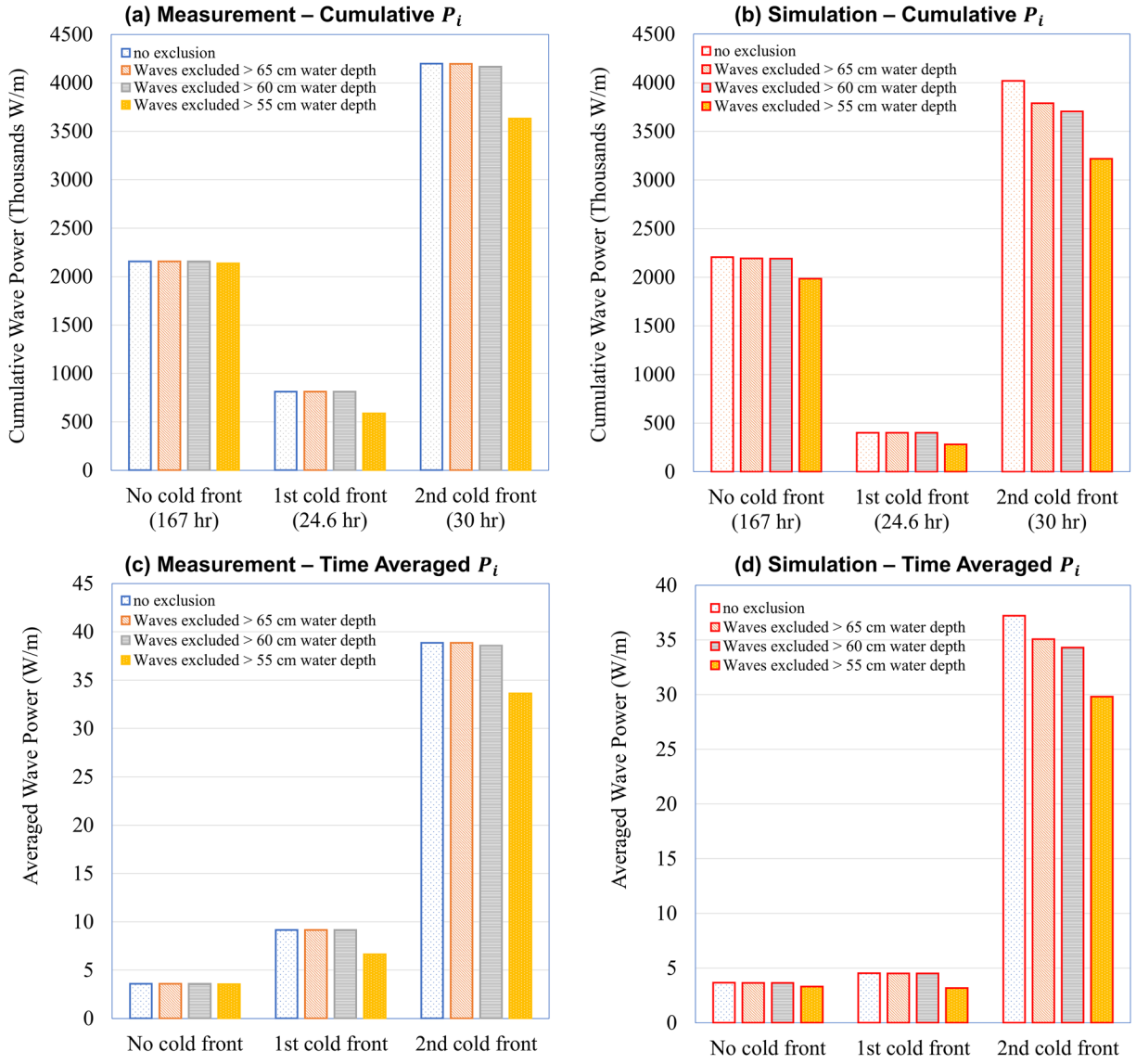

Figure 12. Plot of cumulative effective wave power with different salt marsh platform thresholds in measurement (a) and simulation (b), plot of averaged effective wave power with different salt marsh platform thresholds in measurement (c) and simulation (d).

less cumulative effective wave power of the first cold front to the site of interest even though its bulk wave power was 110% higher than the effective wave power.

On the other hand, the second cold front arrived with moderate wind gusts for a relatively long time, with limited flooding affecting the marsh edges with elevated wave energy over a long duration. Unlike the first cold front, the winds during the postfrontal phase were much higher than that of the prefrontal phase (Figure 6b), which results in a significant effect on the accumulation of wave energy toward the north-facing salt marshes (Figure 12).

The duration of time without a cold front ("no-cold-front" period), the first cold front, and the second cold front were 167, 24.6, and 30 h, respectively. The time-averaged effective wave power of the second cold front was the highest among the three periods, likely due to its duration (Figures 12c and 12d).

In the comparison of the wave power along with the immersion thresholds, there was no sudden cumulative wave power reduction except in the scenario of flooding at 0.55 m. Using estimated flood elevations

of 0.65 and 0.60 m, the effective wave power reduction was minimal, due to the postfrontal winds which contributed to the rapid reduction of the water depth in the Galveston Bay. Therefore, after passing through the cold front, the possibility of flooding is greatly reduced, so that the wave energy can affect the edge of the salt marsh without loss.

Leonardi et al. (2016b) suggested that winter cold fronts called winter storms which accompany strong winds, can lead to more erosion than hurricanes and found that waves with a return period of 2.5 months have the highest effect on salt marsh deterioration. In connection with these findings, additional parameters such as the presence of wind gusts, the wind direction change, and water level change during cold fronts may need to be considered together as factors in determining the cause of wetland erosion in shallow bays.

6. Summary and Conclusions

The model successfully reproduced the observed tides and waves in the relatively shallow depths of West Galveston Bay. This case study demonstrates the effect of cold-front-induced wave and water level amplification on the edge of bounding wetlands. Compared to that of storm surge, the role of seasonal cold fronts and the generated waves on impact and erosion of wetlands has not been as well identified. From the measurement and the model results, the following findings can be derived. First, wind gusts during the cold front passage affect the wave conditions in the area, making its use essential for wind input to models. Furthermore, from the prefrontal phase to the passage of cold frontal edge, an increase in water elevation in the coastal microtidal bay was observed both in first and second cold fronts which are caused by wind-driven currents to the bay during the prefrontal passage. Increased water level changes the wind-wave growth characteristics within the bay from partially depth limited condition to fully fetch limited condition, ensuring additional wave growth. During the passage of frontal edge, increased gustiness of the winds increases the significant wave heights to a level in which the erosion of the salt marsh edge was possible. However, when high tide coincided with the prefrontal phase, the water level in the microtidal bay increased to the point where the inundation of the wetlands occurred, which reduced the possible erosive impact of the generated waves. Additionally, considering the time-averaged wave power of the second cold front, we determined that the cumulative wave power increase at a faster rate when a cold front was moving through the area relatively slowly. Under the assumption that the waves move in line with the wind (applicable for wind-generated waves), the waves during the "no-cold-front" period had no distinct directionality, limiting its impact on the marsh edge.

In contrast, the cold front-induced waves had a clear preferential direction throughout the prefrontal, frontal passage, and postfrontal period. This is indicated by the high cumulative wave power value of the second cold front (4,200,000 W/m) compared to the no-cold-front period (2,150,000 W/m) even though the measurement period of the no-cold-front period (167 h) was much longer than the second cold front (30 h). We confirmed that the second cold front-induced waves had a greater impact on north-facing salt marsh erosion during the frontal passage and postfrontal with its high cumulative wave power in the site of interest. In this study's investigation of cold front induced surge and waves, high gusts and winds from cold fronts increased tide and waves along the shallow bay. The occurrence of gusts and dynamical changes in wind direction during the cold front passage can have a significant impact on changes in water depth, wave amplitude, and ultimately on the potential erosion rate of salt marshes in shallow bays. Considering that the number of times that cold fronts pass per year is higher compared to that of hurricanes, the potential impact on lateral erosion of coastal wetlands is thought to be significant. Moreover, prefrontal winds and postfrontal winds that occur as the cold front passes through can significantly affect the salt marsh edges facing the opposite of their wind directions, evidenced by the postfrontal wind's effect on the north-facing salt marshes in the study. Subsequently, the characteristics of these cold fronts can have a lasting effect on salt marshes in specific locations in shallow bays.

Now that the model has been verified for this application, it can be used to gauge the effect of wave action on barrier island salt marsh, and further also be used to determine the cumulative wave power of the entire cold front passing each year to associate with the annual salt marsh retreat rate. The model can provide wave data to identify the role of wave energy affecting total salt marsh erosion. However, such modeling work could be coupled with extensive field measurements of marsh platform height, soil, and vegetation properties.

Data Availability Statement

The data used in this study can be obtained online at https://doi.org/10.5281/zenodo.3971498 repository.

Acknowledgments
This research was supported by the Texas Sea Grant College Program, National Oceanic and Atmospheric Administration via the project entitled "Study of Wetland Erosion due to Storms through Combined Field, Laboratory, and Numerical Investigations."

References

Alizad, K., Hagen, S. C., Morris, J. T., Medeiros, S. C., Bilskie, M. V., & Weishampel, J. F. (2016). Coastal wetland response to sea-level rise in a fluvial estuarine system. *Earth's Future*, *4*(11), 483–497. http://dx.doi.org/10.1002/2016EF000385

Battjes, J. A., & Janssen, J. (1978). Energy loss and set-up due to breaking of random waves. *Coastal Engineering*, *1978*, 569–587.

Becker, J. J., Sandwell, D. T., Smith, W. H. F., Braud, J., Binder, B., Depner, J., et al. (2009). Global bathymetry and elevation data at 30 arc seconds resolution: SRTM30_PLUS. *Marine Geodesy*, *32*(4), 355–371. https://doi.org/10.1080/01490410903297766

Booij, N., Ris, R., & Holthuijsen, L. H. (1999). A third-generation wave model for coastal regions: 1. Model description and validation. *Journal of Geophysical Research*, *104*(C4), 7649–7666.

Buczkowski, B. J. (2006). *usSEABED: Gulf of Mexico and Caribbean (Puerto Rico and US Virgin Islands) offshore surficial-sediment data release*, Reston, VA: US Department of the Interior, US Geological Survey.

Cahoon, D. R. (2006). A review of major storm impacts on coastal wetland elevations. *Estuaries and Coasts*, *29*(6), 889–898. http://dx.doi.org/10.1007/BF02798648

Cox, D. T., Tissot, P., & Michaud, P. (2002). Water level observations and short-term predictions including meteorological events for entrance of Galveston Bay, Texas. *Journal of Waterway, Port, Coastal, and Ocean Engineering*, *128*(1), 21–29.

Dahl, T. E., & Johnson, C. E. (1991). *Wetlands, status and trends in the conterminous United States, mid-1970's to mid-1980's: First update of the national wetlands status report*, Washington, DC: US Department of the Interior, Fish and Wildlife Service.

Deltares, D. (2013). *Delft3D-FLOW user manual*. Delft, The Netherlands: Deltares Delft.

DiMego, G. J., Bosart, L. F., & Endersen, G. W. (1976). An examination of the frequency and mean conditions surrounding frontal incursions into the Gulf of Mexico and Caribbean Sea. *Monthly Weather Review*, *104*(6), 709–718.

Donatelli, C., Ganju, N. K., Kalra, T. S., Fagherazzi, S., & Leonardi, N. (2019). Changes in hydrodynamics and wave energy as a result of seagrass decline along the shoreline of a microtidal back-barrier estuary. *Advances in Water Resources*, *128*, 183–192.

Donatelli, C., Zhang, X., Ganju, N. K., Aretxabaleta, A. L., Fagherazzi, S., & Leonardi, N. (2020). A nonlinear relationship between marsh size and sediment trapping capacity compromises salt marshes-stability. *Geology*, *48*(10), 966–970.

Duran-Matute, M., Gerkema, T., & Sassi, M. G. (2016). Quantifying the residual volume transport through a multiple-inlet system in response to wind forcing: The case of the western Dutch Wadden Sea. *Journal of Geophysical Research: Oceans*, *121*(12), 8888–8903. https://doi.org/10.1002/2016JC011807

Egbert, G. D., & Erofeeva, S. Y. (2002). Efficient inverse modeling of Barotropic Ocean tides. *Journal of Atmospheric and Oceanic Technology*, *19*(2), 183–204. https://doi.org/10.1175/1520-0426(2002)019<0183:EIMOBO>2.0.CO;2

Entwistle, C., Mora, M. A., & Knight, R. (2018). Estimating coastal wetland gain and losses in Galveston County and Cameron County, Texas, USA. *Integrated Environmental Assessment and Management*, *14*(1), 120–129.

Fagherazzi, S. (2014). Coastal processes: Storm-proofing with marshes. *Nature Geoscience*, *7*(10), 701–702.

Fagherazzi, S., Mariotti, G., Porter, J., McGlathery, K., & Wiberg, P. (2010). Wave energy asymmetry in shallow bays. *Geophysical Research Letters*, *37*(24), L24601. https://doi.org/10.1029/2010GL045254

Fagherazzi, S., & Wiberg, P. (2009). Importance of wind conditions, fetch, and water levels on wave-generated shear stresses in shallow intertidal basins. *Journal of Geophysical Research*, *114*(F3), F03022. https://doi.org/10.1029/2008JF001139

Feagin, R. A., Lozada-Bernard, S., Ravens, T., Möller, I., Yeager, K. M., & Baird, A. (2009). Does vegetation prevent wave erosion of salt marsh edges?. *Proceedings of the National Academy of Sciences*, *106*(25), 10109–10113.

Feagin, R. A., Martinez, M. L., Mendoza-Gonzalez, G., & Costanza, R. (2010). Salt marsh zonal migration and ecosystem service change in response to global sea level rise: A case study from an urban region. *Ecology and Society*, *15*(4), 14.

Gibeaut, J. C., Waldinger, R., Hepner, T., Tremblay, T. A., & White, W. A. (2003). Changes in bay shoreline position, West Bay system, Texas: The University of Texas at Austin, Bureau of Economic Geology. A report of the Texas Coastal Coordination Council pursuant to National Oceanic and Atmospheric Administration Award No. NA07OZ0134. GLO contract No. 02-225R, 27 p.

Hanson, J. L., Tracy, B. A., Tolman, H. L., & Scott, R. D. (2009). Pacific hindcast performance of three numerical wave models. *Journal of Atmospheric and Oceanic Technology*, *26*(8), 1614–1633.

Hasselmann, K., Barnett, T., Bouws, E., Carlson, H., Cartwright, D., Enke, K., et al. (1973). Measurements of wind-wave growth and swell decay during the Joint North Sea Wave Project (JONSWAP). *Ergänzungsheft*, 8–12.

Hasselmann, S., Hasselmann, K., Allender, J., & Barnett, T. (1985). Computations and parameterizations of the nonlinear energy transfer in a gravity-wave spectrum. Part II: Parameterizations of the nonlinear energy transfer for application in wave models. *Journal of Physical Oceanography*, *15*(11), 1378–1391.

Hofland, B., Chen, X., Altomare, C., & Oosterlo, P. (2017). Prediction formula for the spectral wave period Tm-1, 0 on mildly sloping shallow foreshores. *Coastal Engineering*, *123*, 21–28.

Hope, M. E., Westerink, J. J., Kennedy, A. B., Kerr, P., Dietrich, J. C., Dawson, C., et al. (2013). Hindcast and validation of Hurricane Ike (2008) waves, forerunner, and storm surge. *Journal of Geophysical Research: Oceans*, *118*(9), 4424–4460.

Horstman, E., Dohmen-Janssen, M., & Hulscher, S. (2013). Modeling tidal dynamics in a mangrove creek catchment in Delft3D. *Coastal Dynamics*. *2013*, 833–844.

Huff, T. P., Feagin, R. A., & Delgado, A. (2019). Understanding lateral marsh edge erosion with Terrestrial Laser Scanning (TLS). *Remote Sensing*, *11*(19), 2208.

Karimpour, A., Chen, Q., & Twilley, R. R. (2016). A field study of how wind waves and currents may contribute to the deterioration of saltmarsh fringe. *Estuaries and Coasts*, *39*(4), 935–950. http://dx.doi.org/10.1007/s12237-015-0047-z

Keen, T. R. (2002). Waves and currents during a winter cold front in the Mississippi bight, Gulf of Mexico: Implications for Barrier Island Erosion. *Journal of Coastal Research*, *18*(4), 622–636. http://www.jstor.org/stable/4299115

Kerr, P., Donahue, A., Westerink, J. J., Luettich, R., Jr, Zheng, L., Weisberg, R. H., et al. (2013). US IOOS coastal and ocean modeling testbed: Inter-model evaluation of tides, waves, and hurricane surge in the Gulf of Mexico. *Journal of Geophysical Research: Oceans*, *118*(10), 5129–5172. https://doi.org/10.1002/jgrc.20376

Kulawardhana, R. W., Feagin, R. A., Popescu, S. C., Boutton, T. W., Yeager, K. M., & Bianchi, T. S. (2015). The role of elevation, relative sea-level history and vegetation transition in determining carbon distribution in *Spartina alterniflora* dominated salt marshes *Estuarine. Coastal and Shelf Science*, *154*, 48–57.

Leonardi, N., Defne, Z., Ganju, N. K., & Fagherazzi, S. (2016a). Salt marsh erosion rates and boundary features in a shallow Bay. *Journal of Geophysical Research: Earth Surface*, *121*(10), 1861–1875. https://doi.org/10.1002/2016JF003975

Leonardi, N., & Fagherazzi, S. (2015). Effect of local variability in erosional resistance on large-scale morphodynamic response of salt marshes to wind waves and extreme events. *Geophysical Research Letters*, *42*(14), 5872–5879. https://doi.org/10.1002/2015GL064730

Leonardi, N., Ganju, N. K., & Fagherazzi, S. (2016b). A linear relationship between wave power and erosion determines salt-marsh resilience to violent storms and hurricanes. *Proceedings of the National Academy of Sciences*, *113*(1), 64–68.

Lesser, G., Roelvink, J., van Kester, J., & Stelling, G. (2004). Development and validation of a three-dimensional morphological model. *Coastal Engineering*, *51*(8), 883–915. http://www.sciencedirect.com/science/article/pii/S0378383904000870 (Coastal Morphodynamic Modeling) https://doi.org/10.1016/j.coastaleng.2004.07.014

Lester, J., Gonzalez, L. A., Sage, T., & Gallaway, A. (2002). *The state of the bay: A characterization of the Galveston Bay ecosystem. Tech. Rep. Galveston Bay Estuary Program*, Houston, TX: Texas Commission on Environmental Quality.

Liu, K., Chen, Q., Hu, K., Xu, K., & Twilley, R. R. (2018). Modeling hurricane-induced wetland-bay and bay-shelf sediment fluxes. *Coastal Engineering*, *135*, 77–90.

Mann, K. H., & Lazier, J. R. (2013). *Dynamics of marine ecosystems: Biological-physical interactions in the oceans*, Hoboken, NJ: John Wiley & Sons.

Marani, M., D'Alpaos, A., Lanzoni, S., & Santalucia, M. (2011). Understanding and predicting wave erosion of marsh edges. *Geophysical Research Letters*, *38*(21), L21401. https://doi.org/10.1029/2011GL048995

Mathieson, S., Cattrijsse, A., Costa, M., Drake, P., Elliott, M., Gardner, J., & Marchand, J. (2000). Fish assemblages of European tidal marshes: A comparison based on species, families and functional guilds. *Marine Ecology Progress Series*, *204*, 225–242.

McLoughlin, S. M., Wiberg, P. L., Safak, I., & McGlathery, K. J. (2015). Rates and forcing of marsh edge erosion in a shallow coastal bay. *Estuaries and Coasts*, *38*(2), 620–638. https://doi.org/10.1007/s12237-014-9841-2

Möller, I., Kudella, M., Rupprecht, F., Spencer, T., Paul, M., Van Wesenbeeck, B. K., et al. (2014). Wave attenuation over coastal salt marshes under storm surge conditions. *Nature Geoscience*, *7*(10), 727–731.

Möller, I., & Spencer, T. (2002). Wave dissipation over macro-tidal saltmarshes: Effects of marsh edge typology and vegetation change. *Journal of Coastal Research*, *36*(sp1), 506–521.

Moulton, D. W. (1997). *Texas coastal wetlands: Status and trends, mid-1950s to early 1990s*, Albuquerque, NM: US Department of the Interior, Fish and Wildlife Service, Southwestern Region.

NOAA Tides and Currents (2020). *Meteorological observations-measurement specifications*. Retrieved from https://tidesandcurrents.noaa.gov/publications/CO-OPS_Measurement_Spec.pdf

Parker, B., Milbert, D., Hess, K., & Gill, S. (2003). National VDatum–The implementation of a national vertical datum transformation database. *Proceeding from the US Hydro-2003 Conference* (pp. 24–27). Silver Spring, MD.

Priestas, A. M., Mariotti, G., Leonardi, N., & Fagherazzi, S. (2015). Coupled wave energy and erosion dynamics along a salt marsh boundary, Hog Island Bay, Virginia, USA. *Journal of Marine Science and Engineering*, *3*(3), 1041–1065.

Ravens, T. M., Thomas, R. C., Roberts, K. A., & Santschi, P. H. (2009). Causes of salt marsh erosion in Galveston Bay, Texas. *Journal of Coastal Research*, *25*(252), 265–272.

Roberts, H. H., DeLaune, R. D., White, J. R., Li, C., Sasser, C. E., Braud, D., et al. (2015). Floods and cold front passages: Impacts on coastal marshes in a river diversion setting (Wax Lake Delta Area, Louisiana). *Journal of Coastal Research*, *31*(5), 1057–1068.

Roberts, H., Huh, O., Hsu, S., Rouse, L., & Rickman, D. (1987). Impact of cold-front passages on geomorphic evolution and sediment dynamics of the complex Louisiana coast. In N. C. Krause (Ed.), *Coastal sediments '87* (pp. 1950–1963)). New York, NY: American Society of Civil Engineers.

Rogers, W. E., Hwang, P. A., & Wang, D. W. (2003). Investigation of wave growth and decay in the SWAN model: Three regional-scale applications. *Journal of Physical Oceanography*, *33*(2), 366–389.

Saha, S., Moorthi, S., Wu, X., Wang, J., Nadiga, S., Tripp, P., et al. (2014). The NCEP climate forecast system version 2. *Journal of Climate*, *27*(6), 2185–2208. https://doi.org/10.1175/JCLI-D-12-00823.1

Schwimmer, R. A. (2001). Rates and processes of marsh shoreline erosion in Rehoboth Bay, Delaware, USA. *Journal of Coastal Research*, *17*(3), 672–683.

Schwimmer, R. A., & Pizzuto, J. E. (2000). A model for the evolution of marsh shorelines. *Journal of Sedimentary Research*, *70*(5), 1026–1035.

Sebastian, A., Proft, J., Dietrich, J. C., Du, W., Bedient, P. B., & Dawson, C. N. (2014). Characterizing hurricane storm surge behavior in Galveston Bay using the SWAN+ ADCIRC model. *Coastal Engineering*, *88*, 171–181.

Seibt, C., Peeters, F., Graf, M., Sprenger, M., & Hofmann, H. (2013). Modeling wind waves and wave exposure of nearshore zones in medium-sized lakes. *Limnology & Oceanography*, *58*(1), 23–36.

Snyder, R., Dobson, F., Elliott, J., & Long, R. (1981). Array measurements of atmospheric pressure fluctuations above surface gravity waves. *Journal of Fluid Mechanics*, *102*, 1–59.

Taylor, L. A., Eakins, B. W., Carignan, K. S., Warnken, R. R., Sazonova, T., & Schoolcraft, D. C. (2008). *Digital elevation model of Galveston, Texas: Procedures, data sources and analysis*. National Geophysical Data Center National Oceanic and Atmospheric Administration Technical Memorandum NESDIS NGDC-12.

Tilburg, C. E., & Garvine, R. W. (2004). A simple model for coastal sea level prediction. *Weather and Forecasting*, *19*(3), 511–519.

Tonelli, M., Fagherazzi, S., & Petti, M. (2010). Modeling wave impact on salt marsh boundaries. *Journal of Geophysical Research*, *115*(C9), C09028. https://doi.org/10.1029/2009JC006026

Valentine, K., & Mariotti, G. (2019). Wind-driven water level fluctuations drive marsh edge erosion variability in microtidal coastal bays. *Continental Shelf Research*, *176*, 76–89.

van der Wal, D., & Pye, K. (2004). Patterns, rates and possible causes of saltmarsh erosion in the Greater Thames area (UK). *Geomorphology*, *61*(3), 373–391.

Walker, N. D., & Hammack, A. B. (2000). Impacts of winter storms on circulation and sediment transport: Atchafalaya-Vermilion Bay region, Louisiana, USA. *Journal of Coastal Research*, *16*(4), 996–1010.

White, W. A., Tremblay, T. A., Waldinger, R. L., & Calnan, T. R. (2004). *Status and trends of wetland and aquatic habitats on barrier islands, upper Texas Coast, Galveston and Christmas Bays Tech Rep*, Austin, TX: University of Texas at Austin.

Young, I. R., & Verhagen, L. (1996). The growth of fetch limited waves in water of finite depth. Part 1. Total energy and peak frequency. *Coastal Engineering*, *29*(1–2), 47–78.